

Adaptive Smooth Control via Nonsingular Fast Terminal Sliding Modes for Distributed Space Telescope Demonstration Mission by CubeSat Formation Flying

Soobin Jeon

Ph.D Candidate, Department of Astronomy, Yonsei University, Seoul 03722, Republic of Korea

Hancheol Cho

Associate Professor, Department of Astronomy, Yonsei University, Seoul 03722, Republic of Korea
Visiting Assistant Professor, Department of Aerospace Engineering, Embry-Riddle Aeronautical University, Daytona Beach, FL 32114, USA

Sang-Young Park

Professor, Department of Astronomy, Yonsei University, Seoul 03722, Republic of Korea

Abstract— This paper investigates the efficiency of a nonsingular fast terminal sliding mode-based adaptive smooth control method for the distributed space telescope demonstration mission. The distributed space telescope has a flexible focal length that corresponds to the relative position in the formation flying concept. The precise formation flying technology implemented by CubeSats enhances the utility of distributed space systems at low costs. The propulsion systems for CubeSats usually have restricted degrees of freedom. Since the scientific mission requires continuous orbit control, the attitude and orbit control system mutually affect the control performance. The nonsingular fast terminal sliding mode proposed in this study has the advantage of a fast convergence rate and is able to improve the control performance. The adaptive smooth controller previously designed for a single-input, single-output system is extended and applied to the attitude and orbit control system. The simulation results verify the efficiency of the

proposed adaptive smooth controller based on the nonsingular fast terminal sliding mode.

Index Terms— Robust control, Nonsingular fast terminal sliding mode control, Adaptive control, CubeSat, Formation Flying

Nomenclature

$\mathbf{r} = [x \ y \ z]^T$	Relative position vector in the LVLH frame
$\dot{\mathbf{r}} = [\dot{x} \ \dot{y} \ \dot{z}]^T$	Relative velocity vector in the LVLH frame
$\mathbf{q} = [q_v^T \ q_s]^T$	Quaternion
$(\cdot)^i$	A variable or parameter in an inertial frame
$(\cdot)^l$	A variable or parameter in the LVLH frame
$(\cdot)^b$	A variable or parameter in the body frame
$(\cdot)_c$	A variable or parameter of the chief satellite
$(\cdot)_d$	A variable or parameter of the deputy satellite
$(\cdot)_{att}$	A variable or parameter of the attitude control system
$(\cdot)_{orb}$	A variable or parameter of the relative orbit control system
$(\cdot)_r$	Reference, desired, or target variable or parameter
$(\cdot)_e$	Error variable or parameter

I. Introduction

The advancement of satellite development technology has led to the concept of a distributed space system, which aims to substitute medium or large single satellites with a number of small satellites [1]–[3]. The distributed space system is a system that integrates several satellites into a single architecture and encompasses satellite constellations, formation flying, and distributed space telescopes, etc. Distributed space systems offer the capability that strategically organizes the configuration of satellites in accordance with given mission objectives. Hence it contributes to expand the diversity and flexibility of scientific missions utilizing satellites.

The conventional formation flight missions have reference relative trajectories that are designed based on the relative dynamics exhibited by two similar satellites. Therefore, the reference trajectory retains its stability in the absence of a control input. The Gravity Recovery and Climate Experiment (GRACE) and the Gravity Recovery and Climate Experiment Follow-on (GRACE-FO) mission is a scientific mission that quantifies the gravitational field by analyzing alterations in relative motion [4], [5]. TerraSAR-X/TanDEM-X (TSX/TDX) satellites acquire ground observation data regularly by applying instantaneous thrust to maintain relative motion within the control window [6]. The formation flight control technology verification mission either modifies the relative orbit to

Manuscript received XXXXX 00, 0000; revised XXXXX 00, 0000; accepted XXXXX 00, 0000.

Corresponding author: S.-Y. Park

Soobin Jeon is with the Department of Astronomy, Yonsei University, Seoul 03722, Republic of Korea (e-mail: forestine@yonsei.ac.kr). Hancheol Cho is with the Department of Astronomy, Yonsei University, Seoul 03722, Republic of Korea (e-mail: hanchol37@yonsei.ac.kr) and the Department of Aerospace Engineering, Embry-Riddle Aeronautical University, Daytona Beach, FL 32114, USA (e-mail: choh15@erau.edu). Sang-Young Park is with the Department of Astronomy, Yonsei University, Seoul 03722, Republic of Korea (e-mail: spark624@yonsei.ac.kr).

rendezvous (CanX-4/5) or executes inter-satellite docking with proximity operations (CPOD) [7]–[9].

A distributed space telescope is a kind of distributed space system that observes inertial objects by formation flying of dual-spacecraft. The distributed space telescope that is also known as binary-distributed telescope [10] or virtual telescope (VT) [11] refers to a group of multiple satellites equipped with optics and detection payload functions as a single instrument [10]. Distributed telescopes have a variable and extensive local length compared to monolithic telescopes and consist of a number of more compact structures, which has the advantage of relatively low launch and development costs [12]. This paper uses the term distributed space telescope.

Inertial Alignment Hold (IAH) is the technology that maintains a specific configuration for the inertial target in order to implement distributed space telescopes. The relative distance of the formation flying is the telescope's baseline or focal length and is designed to range from 1,000 to 72,000 kilometers (astrophysical targets) [13], [14] to 50 to 500 meters (heliophysical targets and X-ray images) [15], [16], depending on the observation target and wavelength band. In contrast to conventional formation flight missions, the reference trajectories of the inertial alignment hold missions should be designed with the separation of focal lengths with respect to the inertial targets. Since the control law must retain the alignment precisely within the requirements, this paper suggests a robust control approach that compensates for the effects of disturbances using continuous thrust.

The main factors that contribute to disturbances in space are uncertainties in the structural properties and unmodeled perturbation forces [17]. The robust system should be able to resist these effects that are neglected in the design phase while performing the tasks. Several robust control techniques have been proposed and have proven their effectiveness in a variety of practical control problems. One common solution for achieving robustness is sliding mode control (SMC) [18]–[20]. The sliding mode control approach allows the system's states to defy the natural motion and follow the designed trajectory, the so-called 'sliding surface.'

The feasibility of the sliding mode control in formation flying missions has been proven in literature over several decades. The adaptive linear and nonsingular terminal sliding mode control approach achieves submillimeter formation keeping precision even when the operational faults are detected [21]. The continuous and high-order sliding mode controller with consecutive pulse-width modulation was applied to the satellite formation flying in [22]. The sliding mode approach in this application showed high tracking accuracy in the presence of bounded and matched disturbances and uncertainties. The fuzzy-SMC-based technique successfully conducted reconfiguration within a short time span with a minimum control effort for the multiple satellite formation flying problems [23].

The quaternion-based finite-time control technique with a linear sliding surface and nonlinear control law

showed a fast convergent rate and the alleviation of chattering in the attitude synchronization and stabilization problem [24]. The robust sliding mode controller shows its efficiency in electromagnetic formation flight (EMFF) control problems under highly nonlinear environments such as the electromagnetic model and magnetic model uncertainties [25], [26]. In [25], the terminal sliding mode for the relative translational dynamics showed improved performance compared to the linear sliding surface. Another paper [26] applied a linear sliding surface to the relative position and attitude tracking problems and successfully handled the control difficulties of EMFF in close proximity.

In this paper novel nonsingular fast terminal sliding variables for both relative orbit and attitude control systems are designed and their stability is proven based on the Lyapunov theory. The robust smooth adaptive control law compensates for the nonlinearity of the relative orbit and attitude systems. The sliding variable and adaptive control law are verified with high fidelity by applying them to the real CubeSat Formation Flying mission launched in 2021 to demonstrate a distributed space telescope. The paper also suggests the performance metrics to describe the characteristics of the control systems.

The first section describes the historical background of the distributed space telescope and sliding mode control, the contribution of this paper sequentially. Section II describes the concept and the characteristics of the Guidance, Navigation, and Control (GN&C) subsystem of the DST demonstration mission by CubeSats. Based on the mission objectives, the reference relative orbit and attitude control systems are defined. The orbit and attitude control systems are both necessary for a precise formation flying (PFF) system, so the dynamic and kinematic equations for the nominal and error states are suggested in section III. Section IV suggests the sliding variable and robust adaptive control law that are designed based on Lyapunov theory. The control performance for stabilization and tracking problems are described in section V, which verifies the feasibility of the nonsingular terminal sliding mode controls for the CubeSat formation flying mission developed in this paper. Finally, section VI concludes the paper.

II. Mission Description

CANYVAL-C Mission

The CANYVAL (CubeSat Astronomy by NASA and Yonsei using the Virtual ALignment) project is a distributed space telescope demonstration mission by the formation flying of 1U and 2U CubeSats and was developed by Yonsei University and National Aeronautics and Space Administration (NASA). The 1U satellite is a DSC (Detector Spacecraft) equipped with a visible wavelength camera, and an OSC (Optics Spacecraft), 2U satellite, is equipped with an occulter and operates the propulsion system to perform orbit control. The nonlinear equation of the relative motion that regards the Earth as a point

mass describes the relative states between 1U as the chief and 2U as the deputy.

The configuration based on the mission concept is described in Fig.1. The first phase of the CANYVAL project is CANYVAL-X (CANYVAL-eXperimental) launched in 2018, and the OSC controls only the alignment angle (θ_{align}) in Fig.1 so that it has a flexible separation between DSC and OSC [27]. The second phase of the CANYVAL project is CANYVAL-C (CANYVAL-Coronagraph) launched in 2021, and the thruster has a greater degree of freedom to implement the distributed space telescope with a fixed distance of 40 meters [28]. Therefore the formation flying system controls the errors between the relative position of OSC (\mathbf{r}) and the desired trajectory (\mathbf{r}_r) to complete the DSC – OSC – Sun configuration.

Fig.2a describes the location and orientation of the payload and propulsion system and this configuration requires the attitude maneuver strategy to fire the desired thrust as in Fig.2b. The desired thrust vector $\mathbf{u}_{orb,r}$ at the moment is projected onto the xy -plane, and then the attitude control system generates control torques that match the projected thrust vector $\mathbf{u}'_{orb,r}$ to the desired one. The CANYVAL-C mission's propulsion system utilizes GomSpace's Nanoprop, which fires cold gas through four nozzles in the $\pm\hat{\mathbf{b}}_x$ and $\pm\hat{\mathbf{b}}_y$ directions of the body fixed frame. The occulter is located and points the $-\hat{\mathbf{b}}_z$ that is normal to the thrust nozzles and it constrains the controllable directions in the local-vertical, local-horizontal (LVLH) frame during alignment to the sun. The propulsion system controls only the satellite's orbit, while the attitude is controlled by a reaction wheel assembly composed of three reaction wheels, and excessive revolutions per minute (rpm) are detumbled by magnetorquers. The orbit and attitude control accuracies are dependent on each other because the precise formation flying mission

is executed with the use of continuous thrust of the propulsion system with two degrees of freedom.

Mission Objectives

Since the eclipse and daylight time are repeated alternatively for sun-synchronous orbit (SSO), it is recommended to start to take photos of the solar corona during daylight time while the initial condition is unpredictable. Therefore, the inertial alignment hold is divided into staging and alignment modes and they are executed sequentially for an efficient operation. The primary objective of the staging mode is to reconfigure the satellite in the Projected Circular Orbit (PCO) to an Along-track Orbit (ATO) of a 40-meter along-track distance until sunrise. Even though the position of the sun varies according to the local time of ascending node (LTAN), the along-track orbit is always a good choice because it does not waste fuel consumption. As a result, the reference relative orbit trajectory of the staging mode is defined and described in the LVLH frame as:

$$\mathbf{r}_r = [0 \quad 40 \quad 0]^T \quad (\text{m}) \quad (1)$$

where x -axis radially points the satellite from the center of the Earth, z -axis is normal to the orbital plane and has a positive sign along the instantaneous orbital angular momentum vector, and y -axis completes the right-handed coordinate frame.

When the sun sensor detects the sunlight, the alignment mode is initiated, and the deputy is aligned at a 40-meter distance from the chief toward the sun. The occulter orients to the sun and it constraints the firing direction. Therefore the reference position is derived as:

$$\mathbf{r}_r = 40 \cdot \frac{\mathbf{r}_\odot}{\|\mathbf{r}_\odot\|} \quad (\text{m}) \quad (2)$$

where \mathbf{r}_\odot is the sun vector that orients from 1U to the sun and is described in the LVLH frame.

Fig.4 describes the reference orbital trajectories in the LVLH frame. Since the reference trajectory of the staging mode is a single point by Eq. (1), it is expressed as a cross mark in Fig.4. On the other hand, the epoch time and LTAN determine the reference trajectory of the alignment mode because it depends on the position of the sun by Eq. (2). The Fig.4 shows the reference trajectory of LTAN 11:00 at the vernal equinox in which the satellites were planned to be operated for the CANYVAL-C mission.

The reference attitude is derived from the TRIAD algorithm that defines a coordinate frame with two vectors described in the reference and body frames [29], [30]:

$$\mathbf{C}^b \cdot (\mathbf{C}^i)^T = \mathbf{C}_i^b \quad (3)$$

where the superscript b, i of the direction cosine matrix \mathbf{C} refers to the body and reference frame, respectively. Given the two vectors \mathbf{r}_p and \mathbf{r}_s , the direction cosine matrix is derived as

$$\mathbf{C} = [\hat{\mathbf{r}}_1 \quad \hat{\mathbf{r}}_2 \quad \hat{\mathbf{r}}_3] \quad (4)$$

where $\hat{\mathbf{r}}_1 = \mathbf{r}_p / \|\mathbf{r}_p\|$, $\hat{\mathbf{r}}_2 = \mathbf{r}_p \times \mathbf{r}_s / \|\mathbf{r}_p \times \mathbf{r}_s\|$, and $\hat{\mathbf{r}}_3 = \mathbf{r}_p \times (\mathbf{r}_p \times \mathbf{r}_s) / \|\mathbf{r}_p \times (\mathbf{r}_p \times \mathbf{r}_s)\|$.

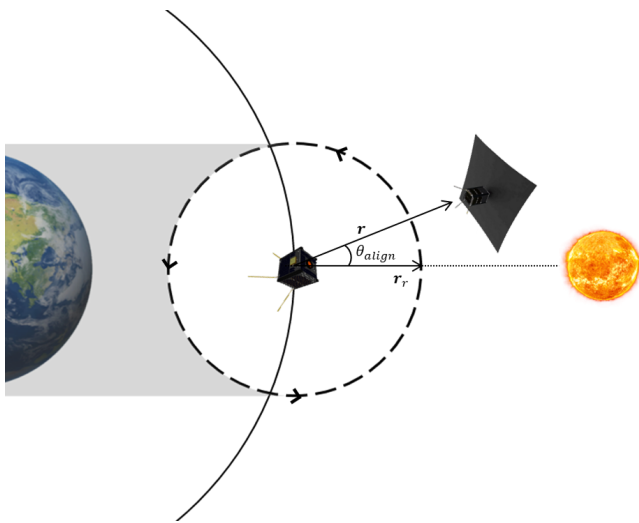


Fig. 1. Distributed space telescope configuration to demonstrate the solar coronagraph

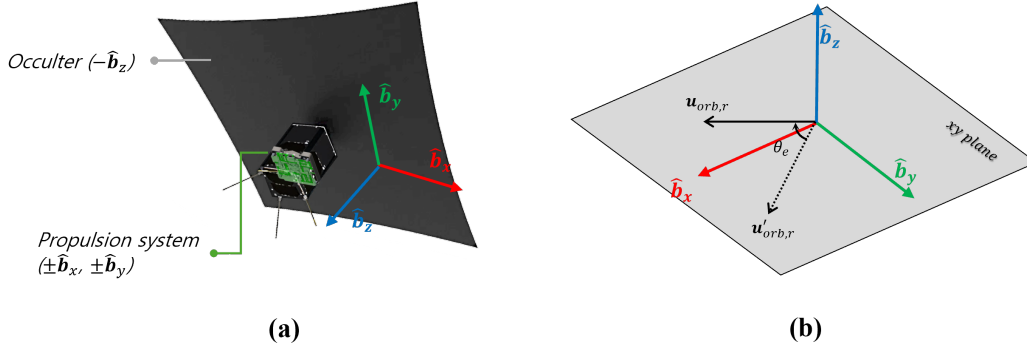


Fig. 2. (a) Location and orientation of the occulter and propulsion system in body frame. (b) Attitude maneuver to compensate for two degrees of freedom of the propulsion system.

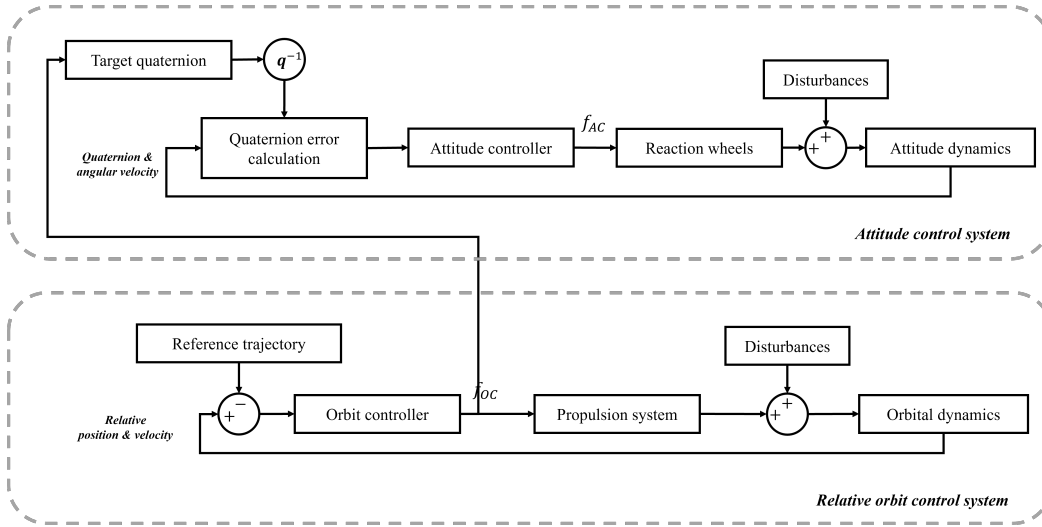


Fig. 3. Block diagram of formation flying system

The quaternion that is also known as the Euler parameters is defined by

$$q_v = a \sin(\theta/2), \quad q_4 = \cos(\theta/2) \quad (5)$$

where a and θ are the Euler axis and the rotation angle about the Euler axis [31], [32].

If q_4 is not zero, the quaternion is able to be derived from the direction cosine matrix as follows [31], [32]:

$$q_v = \frac{1}{4q_4} [C_{23} - C_{32} \quad C_{31} - C_{13} \quad C_{12} - C_{21}]^T \quad (6)$$

$$q_4 = \frac{1}{2} (1 + C_{11} + C_{22} + C_{33})^{\frac{1}{2}} \quad (7)$$

where $C = [C_{ij}]$.

The objective of the staging mode is to control the relative orbit only, so the attitude is controlled to track the reference thrust vector. Hence, the primary and secondary

vectors in the inertial and body frames during the staging mode to define the reference attitude are:

$$r_p^i = u^i, \quad r_s^i = r_{\odot}^i \quad (8)$$

$$r_p^b = [1/\sqrt{2} \quad 1/\sqrt{2} \quad 0]^T \quad (9)$$

$$r_s^b = [0 \quad 0 \quad -1]^T \quad (10)$$

where u^i is the control input, r_{\odot}^i is the sun vector, and both are described in the earth-centered inertial frame.

On the other hand, the primary vector of the attitude control in the alignment mode is to orient the occulter toward the sun. Since the propulsion system has nozzles only along the x and y directions in the body frame, it rotates 10 degrees with respect to the y direction as an ad-hoc strategy. Therefore, the vectors that define the reference attitude frame during the alignment mode are:

$$r_p^i = r_{\odot}^i, \quad r_s^i = C_l^i \cdot [0 \quad 0 \quad 1]^T \quad (11)$$

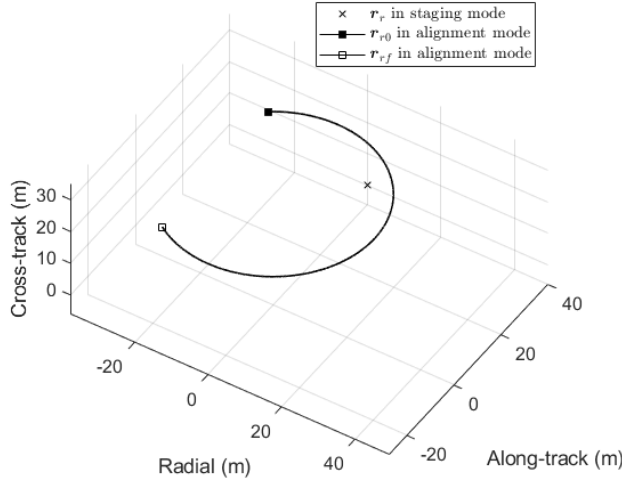


Fig. 4. Reference trajectories described in LVLH frame (cross mark: the reference state in staging mode, filled and empty square: the initial and final reference states in alignment mode, solid line: the reference trajectory in alignment mode)

$$\mathbf{r}_p^b = [0 \quad \pm \sin \theta \quad -1 - \cos \theta]^T \quad (12)$$

$$\mathbf{r}_s^b = [1 \quad 0 \quad 0]^T \quad (13)$$

where \mathbf{C}_l^i is the rotation matrix from the LVLH frame to the inertial frame, θ is the rotation angle that is set as 10 degrees, and the plus sign of \mathbf{r}_p^b indicates that the y and z components of the thrust vector have the same sign. The secondary vectors in the inertial and body frames are derived from the angle β of the sun-synchronous orbit that is the angle between the orbital plane and the sun vector. If the LTAN is supposed to be around 12:00, any normal direction of \mathbf{r}_p^b is recommended to point to the cross-track direction.

III. Description of Formation Flying System

This paper assumes that the propulsion system has two degrees of freedom and controls only the orbital states, and the ACS (Attitude Control System) consists of reaction wheels and magnetorquers. Therefore, the attitude actuator controls the body frame so that the resultant fired thrust vector is aligned with the reference thrust vector in advance of the orbital actuator's firing. The relative orbital dynamics is described in the LVLH coordinate system, defined based on point mass gravity. The quaternions and angular velocity represent the attitude and the dynamic models and the dynamic equation includes the rotational motion of the reaction wheels.

A. Relative Orbit Control System

The Keplerian two-body equations of motion of the chief satellite in the inertial spherical coordinates are

given by [34]

$$\ddot{\mathbf{r}}_c = -\frac{\mu \mathbf{r}_c}{r_c^3} \quad (14)$$

where $\mathbf{r}_c = [r_c \ 0 \ 0]^T$ is the chief's position in the LVLH frame and μ is the standard gravitational parameter of the Earth.

The relative position and the acceleration of the deputy satellite with respect to the chief are defined as

$$\mathbf{r} = \mathbf{r}_d - \mathbf{r}_c \quad (15)$$

$$\ddot{\mathbf{r}} = \ddot{\mathbf{r}}_d - \ddot{\mathbf{r}}_c = -\frac{\mu(\mathbf{r} + \mathbf{r}_c)}{(r + r_c)^3} + \frac{\mu \mathbf{r}_c}{r_c^3} \quad (16)$$

where $\mathbf{r}_d = [r_d \ 0 \ 0]^T = [r + r_c \ 0 \ 0]^T$ is the inertial position of the deputy satellite.

The second time derivative of the position vector in the LVLH frame (l) relative to the inertial frame (i) is

$$\ddot{\mathbf{r}} = \frac{d^2 \mathbf{r}}{dt^2} + 2 {}^i \boldsymbol{\omega}^l \times \frac{d \mathbf{r}}{dt} + \frac{d {}^i \boldsymbol{\omega}^l}{dt} \times \mathbf{r} + {}^i \boldsymbol{\omega}^l \times ({}^i \boldsymbol{\omega}^l \times \mathbf{r}) \quad (17)$$

where ${}^i \boldsymbol{\omega}^l$ is the angular velocity vector of the frame l with respect to the frame i . It is defined as ${}^i \boldsymbol{\omega}^l = [0 \ 0 \ \dot{\theta}_c]^T$ due to its normality to the orbital plane where $\dot{\theta}_c$ is chief's the orbital angular speed.

Therefore, the relative equations of motion are derived as

$$\ddot{\mathbf{r}} = \mathbf{A}_1 \mathbf{r} + \mathbf{A}_2 \dot{\mathbf{r}} + \mathbf{f} + \frac{1}{m} \bar{\mathbf{B}} (\mathbf{u}_{orb} + \mathbf{d}_{orb}) \quad (18)$$

where the nonlinearity of the keplerian motion \mathbf{f} , the matrices \mathbf{A}_1 , \mathbf{A}_2 , and $\bar{\mathbf{B}}$ are defined as

$$\mathbf{A}_1 = \begin{bmatrix} \dot{\theta}^2 - \frac{\mu}{r_d^3} & \ddot{\theta} & 0 \\ -\ddot{\theta} & \dot{\theta}^2 - \frac{\mu}{r_d^3} & 0 \\ 0 & 0 & -\frac{\mu}{r_d^3} \end{bmatrix}, \quad \mathbf{A}_2 = \begin{bmatrix} 0 & 2\dot{\theta} & 0 \\ -2\dot{\theta} & 0 & 0 \\ 0 & 0 & 0 \end{bmatrix}$$

$$\mathbf{f} = \begin{bmatrix} \frac{\mu}{r_c^2} - \frac{\mu r_c}{r_d^3} \\ 0 \\ 0 \end{bmatrix}, \quad \bar{\mathbf{B}} = \begin{bmatrix} 1 & 0 & 0 \\ 0 & 1 & 0 \\ 0 & 0 & 1 \end{bmatrix} \quad (19)$$

and m is the mass of the deputy, θ is the true anomaly of the deputy, $\mathbf{u}_{orb} = [u_{orb,x} \ u_{orb,y} \ u_{orb,z}]^T$ is the orbital control input, and $\mathbf{d}_{orb} = [d_{orb,x} \ d_{orb,y} \ d_{orb,z}]^T$ is the external disturbance force. The mass m is assumed to have uncertainty as described in section IV.

Let the tracking error for the relative orbital states be defined by subtracting the reference state \mathbf{r}_r from the current state \mathbf{r} :

$$\mathbf{r}_e = \mathbf{r} - \mathbf{r}_r = [x - x_r \quad y - y_r \quad z - z_r]^T \quad (20)$$

where $\mathbf{r}_e = [x_e \ y_e \ z_e]^T$.

Hence, the equations of motion of the orbital errors are derived by substituting Eq. (20) into Eq. (18) as

$$\ddot{\mathbf{r}}_e = \mathbf{A}_1 (\mathbf{r}_e + \mathbf{r}_r) + \mathbf{A}_2 (\dot{\mathbf{r}}_e + \dot{\mathbf{r}}_r) + \mathbf{f} + \frac{1}{m} \bar{\mathbf{B}} (\mathbf{u}_{orb} + \mathbf{d}_{orb}) - \ddot{\mathbf{r}}_r \quad (21)$$

where $\dot{\mathbf{r}}_e$ and $\ddot{\mathbf{r}}_e$ are the first and second-time derivatives of the tracking error and $\ddot{\mathbf{r}}_r$ is the second-time derivative of the reference trajectory.

B. Attitude Control System

The kinematic differential equation for the quaternions and the angular velocity that represents the attitude control system of the satellite is written as follows [35]

$$\dot{\mathbf{q}} = \begin{bmatrix} \dot{q}_v \\ \dot{q}_4 \end{bmatrix} = \frac{1}{2} \begin{bmatrix} q_4 \mathbf{I}_{3 \times 3} + \mathbf{q}^\times & \mathbf{q}_v \\ -\mathbf{q}_v^T & q_4 \end{bmatrix} \begin{bmatrix} \boldsymbol{\omega} \\ 0 \end{bmatrix} = \frac{1}{2} \boldsymbol{\Gamma}(\mathbf{q}) \begin{bmatrix} \boldsymbol{\omega} \\ 0 \end{bmatrix} \quad (22)$$

where the quaternions $\mathbf{q} = [\mathbf{q}_v^T \ q_4]^T$ consists of the vector $\mathbf{q}_v = [q_1 \ q_2 \ q_3]^T$ and scalar $\omega = [\omega_1 \ \omega_2 \ \omega_3]^T$ components, $\mathbf{I}_{3 \times 3}$ is the 3 by 3 identity matrix, and the skew-symmetric matrix \mathbf{q}^\times is defined as

$$\mathbf{q}^\times = \begin{bmatrix} 0 & -q_3 & q_2 \\ q_3 & 0 & -q_1 \\ -q_2 & q_1 & 0 \end{bmatrix} \quad (23)$$

The attitude dynamical equations of motion with the control torque generated by the reaction wheels under the external disturbances can be expressed as

$$\mathbf{J}\dot{\boldsymbol{\omega}} = -\boldsymbol{\omega} \times (\mathbf{J}\boldsymbol{\omega} + \mathbf{J}_w \boldsymbol{\omega}_w) + \mathbf{u}_{att} + \mathbf{d}_{att} \quad (24)$$

where \mathbf{J} are the moment of inertia, the subscript w refers to the variables related to the reaction wheels, \mathbf{u}_{att} is the control torque and \mathbf{d}_{att} is the external disturbance torque.

The rotation formula from the current body axes to the reference body axes constructs the attitude tracking error quaternion [30], [32], [35]–[39]

$$\mathbf{q}_e = \begin{bmatrix} \mathbf{q}_{ev} \\ q_{e4} \end{bmatrix} = \begin{bmatrix} q_{r4}\mathbf{q}_v - q_4\mathbf{q}_{rv} - \mathbf{q}_{rv}^\times \mathbf{q}_v \\ q_4q_{r4} + \mathbf{q}_{rv}^T \mathbf{q}_v \end{bmatrix} \quad (25)$$

where $\mathbf{q}_r = [\mathbf{q}_{rv} \ q_{r4}]^T$ is the reference attitude trajectory and $\mathbf{q} = [\mathbf{q}_v^T \ q_4]^T$ is the current attitude.

The angular velocity error is derived as [32], [35], [36], [38], [39]

$$\boldsymbol{\omega}_e = \boldsymbol{\omega} - \mathbf{C}_r^b \boldsymbol{\omega}_r \quad (26)$$

where $\boldsymbol{\omega} = [\omega_1 \ \omega_2 \ \omega_3]^T$ is the current angular velocity and $\boldsymbol{\omega}_r = [\omega_{r1} \ \omega_{r2} \ \omega_{r3}]^T$ is the reference angular velocity.

The matrix \mathbf{C}_r^b represents a rotation matrix from the reference to the current frame and can be expressed for the error quaternion as

$$\mathbf{C}_r^b = (q_{e4}^2 - 2\mathbf{q}_{ev}^T \mathbf{q}_{ev}) \mathbf{I}_{3 \times 3} + 2\mathbf{q}_{ev} \mathbf{q}_{ev}^T - q_{e4} \mathbf{q}_{ev}^\times \quad (27)$$

where $\|\mathbf{C}_r^b\| = 1$ and the derivative of the rotation matrix can derive the angular rate of the body fixed frame as

$$\dot{\mathbf{C}}_r^b = -\boldsymbol{\omega}_e^\times \mathbf{C}_r^b \quad (28)$$

Hence, the error kinematics and dynamic equations are written as [32], [35], [36], [38], [39]

$$\begin{aligned} \dot{\mathbf{q}}_e &= \begin{bmatrix} \dot{\mathbf{q}}_{ev} \\ \dot{q}_{e4} \end{bmatrix} = \frac{1}{2} \begin{bmatrix} q_{e4} \mathbf{I}_{3 \times 3} + \mathbf{q}_{ev}^\times & \mathbf{q}_{ev} \\ -\mathbf{q}_{ev}^T & q_{e4} \end{bmatrix} \begin{bmatrix} \boldsymbol{\omega}_e \\ 0 \end{bmatrix} \\ &= \frac{1}{2} \boldsymbol{\Gamma}(\mathbf{q}_e) \begin{bmatrix} \boldsymbol{\omega}_e \\ 0 \end{bmatrix} \end{aligned} \quad (29)$$

$$\dot{\boldsymbol{\omega}}_e = \mathbf{J}^{-1} \begin{bmatrix} -(\boldsymbol{\omega}_e + \mathbf{C}_r^b \boldsymbol{\omega}_r) \times (\mathbf{J}(\boldsymbol{\omega}_e + \mathbf{C}_r^b \boldsymbol{\omega}_r) + \mathbf{J}_w \boldsymbol{\omega}_w) + \mathbf{u}_{att} + \mathbf{d}_{att} \\ +\mathbf{J}(\boldsymbol{\omega}_e^\times \mathbf{C}_r^b \boldsymbol{\omega}_r - \mathbf{C}_r^b \dot{\boldsymbol{\omega}}_r) \end{bmatrix} \quad (30)$$

C. Problem Statement

To summarize sections II and III, the relative orbit control problem of the CANYVAL-C mission is simplified as two applications: stabilization (staging mode) and tracking problem (alignment mode). The objective of this paper is to design a sliding surface and a control law for the formation flying system so that the errors of the relative orbit and attitude achieve zero in finite time, that is:

$$\lim_{t \rightarrow t_f} (\mathbf{r} - \mathbf{r}_r) = \mathbf{0} \quad (31)$$

$$\lim_{t \rightarrow t_f} (\dot{\mathbf{r}} - \dot{\mathbf{r}}_r) = \mathbf{0} \quad (32)$$

$$\lim_{t \rightarrow t_f} (q_{r4}\mathbf{q}_v - q_4\mathbf{q}_{rv} - \mathbf{q}_{rv}^\times \mathbf{q}_v) = \mathbf{0} \quad (33)$$

$$\lim_{t \rightarrow t_f} (\boldsymbol{\omega} - \mathbf{C}_r^b \boldsymbol{\omega}_r) = \mathbf{0} \quad (34)$$

where the t_f is the finite time that the error converges to the region and the errors are defined in section III.

IV. Control System Design

Assumption 1. The state vectors of the satellite $(\mathbf{r}, \dot{\mathbf{r}}, \mathbf{q}_v, \boldsymbol{\omega})$ are measurable and available throughout the spaceflight mission.

Assumption 2. The uncertain structural properties in the orbit and attitude control systems are the mass and moment of inertia that have unknown lower and upper bounds. In this paper, the mass and moment of inertia are supposed to be bounded as

$$m = m_0 + \delta m \quad (35)$$

$$\mathbf{J} = \mathbf{J}_0 + \delta \mathbf{J} \quad (36)$$

where the subscripts '0' and δ denote the nominal (known) and uncertain values of the variable, respectively.

Assumption 3. The external disturbances are perturbations that include the asymmetric gravity of the Earth, atmospheric drag, and solar radiation pressure. They induce disturbance forces and torques but are bounded by unknown values:

$$0 < d_f < \|\mathbf{d}_{orb}\| < D_f \quad (37)$$

$$0 < d_\tau < \|\mathbf{d}_{att}\| < D_\tau \quad (38)$$

where (d_f, D_f) and (d_τ, D_τ) are the lower and upper bounds of the orbital and attitude disturbances respectively, and are unknown.

Adaptive control law

The adaptive smooth control law is based on sliding mode control and drives the sliding variable into the user-specified domain without the chattering phenomenon. The control law is proposed for the formation flying control system as follows [40]:

$$\mathbf{u}(t) = -\frac{K(t)}{\varepsilon} \mathbf{s}(t) \quad (39)$$

where $K(t)$ is the time-varying gain that obeys the adaptive law defined in Eq. (40), $\mathbf{s}(t)$ is the sliding surface

that will be defined later in this section, and ε is a user-specified positive constant.

The gain is updated by the adaptation law proposed in [40] as follows:

$$\dot{K}(t) = \eta \left(\|u(t)\|_p - K(t) + K_0 \right), K(0) \geq K_0 \quad (40)$$

where $u(t)$ is the adaptive smooth control law in Eq. (39), η is a user-specified positive constant, and K_0 is the lower bound of the control gain that is positive and user-specified and $\|\cdot\|_p$ is a vector p-norm. With this adaptation law, the p-norm of the sliding variable is bounded by ε .

A. Relative Orbit Control System

Sliding variable design

The sliding variable for the relative orbit control system is designed based on nonsingular fast terminal sliding mode as follows:

$$s_{orb}(t) = \dot{r}_e(t) + \alpha_{orb} \text{sig}^{\rho_{orb}} r_e(t) + \beta_{orb} r_e(t) \quad (41)$$

where $\rho_{orb} \in (1, 2)$, $\alpha_{orb} = \text{diag} \{ \alpha_{orb,1}, \alpha_{orb,2}, \alpha_{orb,3} \}$, $\beta_{orb} = \text{diag} \{ \beta_{orb,1}, \beta_{orb,2}, \beta_{orb,3} \}$ are user-specified positive constants where $\alpha_{orb,i=1,2,3} > 0$ and $\beta_{orb,i=1,2,3} > 0$. Besides, $\text{sig}^\rho \xi = [|\xi_1|^\rho \text{sgn}(\xi_1) \quad |\xi_2|^\rho \text{sgn}(\xi_2) \quad |\xi_3|^\rho \text{sgn}(\xi_3)]^T$ for a vector $\xi = [\xi_1 \quad \xi_2 \quad \xi_3]^T$. The subscript and arguments of the various quantities will be suppressed in this section for brevity unless required.

Lemma 1. Suppose a continuous positive definite function $V : \mathbb{R}^n \rightarrow \mathbb{R}$ for a continuous system $\dot{x} = f(x)$, $f(0) = 0$, and $x \in \mathbb{R}^n$. The extended Lyapunov finite-time stability description guarantees the stability of the origin as

$$\dot{V}(x) + aV(x) + bV^m(x) \leq 0, \quad x \in U_0 \quad (42)$$

where $a \in \mathbb{R}^+$, $b \in \mathbb{R}^+$, $m \in (0, 1)$, and $U_0 \subseteq \mathbb{R}^n$ is an open neighborhood of the origin. The finite convergence time is achieved as

$$t \leq \frac{1}{a(1-m)} \ln \frac{aV^{1-m}(x_0) + b}{b} \quad (43)$$

where $x(0) = x_0$ [41].

Proposition 1. The relative position and velocity errors (r_e, \dot{r}_e) are asymptotically stable if the sliding variable s defined in Eq. (41) is zero.

Proof:

Let the Lyapunov candidate be defined as

$$V(t) = \frac{1}{2} r_e^T(t) r_e(t) \quad (44)$$

The time derivative of the orbital sliding variable yields

$$\dot{s}(t) = \ddot{r}_e(t) + \alpha \rho \mathbf{R} \dot{r}_e(t) + \beta \dot{r}_e(t) \quad (45)$$

where $\mathbf{R} = \text{diag} \{ |x_e|^{\rho-1}, |y_e|^{\rho-1}, |z_e|^{\rho-1} \}$.

The time derivative is derived as

$$\begin{aligned} \dot{V} &= r_e^T \dot{r}_e \\ &= r_e^T (-\alpha \text{sig}^\rho r_e - \beta r_e) \\ &\leq \alpha_{\min} \|r_e\|_2^{\rho+1} + \beta_{\min} \|r_e\|_2^2 \\ &= -\alpha_{\min} V^{\frac{\rho+1}{2}} - \beta_{\min} V \end{aligned} \quad (46)$$

where $s = 0$ is used, $\alpha_{\min} = \min_{i=1,2,3} \alpha_i$ and $\beta_{\min} = \min_{i=1,2,3} \beta_i$.

Hence when the sliding variable is maintained to be zero, the orbital error states also converge to zero asymptotically by lemma 1. ■

Lemma 2. Consider V is a C^1 smooth positive definite function that is defined on $U \subset \mathbb{R}^n$. If $\dot{V} + cV^r$ is a negative semi definite function where $c \in \mathbb{R}^+$ and $r \in (0, 1)$, then there exists a region $U_0 \subset \mathbb{R}^n$ such that V can approach zero in finite time from the initial value V_0 on the region U_0 . The convergence time is known as $t \leq \frac{V_0^{1-r}}{c(1-r)}$ [42]–[46].

Theorem 1. Consider the relative orbit control system that is nonlinear and uncertain Eq. (18) with the adaptive smooth feedback control Eqs. (39-40) where p in the adaptive law is 2 and the sliding manifold is designed as Eq. (41). If $\|s\|_2 > \varepsilon$, then the orbital states converge to the region $\|s\|_2 \leq \varepsilon$ in a finite time.

Proof:

Let us define the Lyapunov function $V(t)$ as

$$V(t) = \frac{1}{2} s^T(t) s(t) + \frac{1}{2} \frac{(K(t) - K_{orb}^*)^2}{\gamma_{orb}} \quad (47)$$

where γ_{orb} and K_{orb}^* are positive constants and K_{orb}^* is sufficiently large.

The time derivative is derived as

$$\dot{V} = s^T \dot{s} + \frac{1}{\gamma} (K - K^*) \dot{K} \quad (48)$$

Substituting Eq. (45) and Eq. (21) into Eq. (48) yields

$$\begin{aligned} \dot{s} &= \mathbf{A}_1 (r_e + r_r) + \mathbf{A}_2 (\dot{r}_e + \dot{r}_r) + f + \frac{1}{m} \bar{\mathbf{B}} (u + d) \\ &\quad - \ddot{r}_r + \alpha \rho \mathbf{R} \dot{r}_e + \beta \dot{r}_e \end{aligned} \quad (49)$$

The terms in Eq. (49) are grouped in brackets according to their uncertainties

$$\begin{aligned} \dot{s} &= [\mathbf{A}_1 (r_e + r_r) + \mathbf{A}_2 (\dot{r}_e + \dot{r}_r) + f - \ddot{r}_r + \alpha \rho \mathbf{R} \dot{r}_e + \beta \dot{r}_e] \\ &\quad + \frac{1}{m} \bar{\mathbf{B}} d + \frac{1}{m} \bar{\mathbf{B}} u \end{aligned} \quad (50)$$

With Eq. (19), the time derivative of the sliding variable simply leads to

$$\dot{s} = \frac{1}{m} u + \bar{\mathbf{D}} \quad (51)$$

where $\bar{\mathbf{D}} = [\mathbf{A}_1 (r_e + r_r) + \mathbf{A}_2 (\dot{r}_e + \dot{r}_r) + f - \ddot{r}_r + \alpha \rho \mathbf{R} \dot{r}_e + \beta \dot{r}_e] + \frac{1}{m} \bar{\mathbf{B}} d$ includes the nonlinearities of the dynamics and uncertainties with the unknown upper bound $\|\bar{\mathbf{D}}\|_2 < \Gamma$. Assume that K^* is selected such that $K^* > m_{\max} \Gamma$ and $K^* > K(t)$ for all time $t \geq 0$ and $K(t)$ is bounded [40],

then

$$\begin{aligned}
\dot{V} &= \mathbf{s}^T \dot{\mathbf{s}} + \frac{1}{\gamma} (K - K^*) \dot{K} \\
&= \mathbf{s}^T \left(\bar{\mathbf{D}} + \frac{1}{m} \mathbf{u} \right) + \frac{1}{\gamma} (K - K^*) \dot{K} \\
&= \mathbf{s}^T \left(\bar{\mathbf{D}} - \frac{K}{m\varepsilon} \mathbf{s} \right) + \frac{1}{\gamma} (K - K^*) \dot{K} \\
&< \|\mathbf{s}\|_2 \Gamma - \frac{K}{m\varepsilon} \mathbf{s}^T \mathbf{s} + \frac{1}{\gamma} (K - K^*) \dot{K} \\
&= \frac{\|\mathbf{s}\|_2}{m} \left(m\Gamma - \frac{K}{\varepsilon} \|\mathbf{s}\|_2 \right) + \frac{1}{\gamma} (K - K^*) \dot{K}
\end{aligned} \tag{52}$$

where m_{max} is the maximum value of the uncertain mass. Let us assume the case where the sliding variable stays in the region $\|\mathbf{s}\|_2 > \varepsilon$. Then Eq. (52) is derived as

$$\begin{aligned}
\dot{V} &< \frac{\|\mathbf{s}\|_2}{m} (m\Gamma - K) + \frac{1}{\gamma} (K - K^*) \dot{K} - \frac{\|\mathbf{s}\|_2}{m} K^* \\
&= \frac{\|\mathbf{s}\|_2}{m} (m\Gamma - K^*) + \frac{1}{\gamma} (K - K^*) \dot{K} - \frac{\|\mathbf{s}\|_2}{m} (K - K^*) \\
&< \frac{\|\mathbf{s}\|_2}{m_{min}} (m_{max}\Gamma - K^*) + \frac{1}{\gamma} (K - K^*) \dot{K} - \frac{\|\mathbf{s}\|_2}{m} (K - K^*) \text{ as} \\
&= -\lambda_s \|\mathbf{s}\|_2 - |K - K^*|_2 \left(-\frac{\|\mathbf{s}\|_2}{m} + \frac{1}{\gamma} \dot{K} \right)
\end{aligned} \tag{53}$$

where $\lambda_s \triangleq \frac{K^* - m_{max}\Gamma}{m_{min}}$ is defined and the equality condition $K - K^* = -|K - K^*|$ is utilized. Now, a new parameter λ_K is introduced such that

$$\begin{aligned}
\dot{V} &< -\lambda_s \|\mathbf{s}\|_2 - |K - K^*| \left(-\frac{\|\mathbf{s}\|_2}{m} + \frac{1}{\gamma} \dot{K} \right) + \lambda_K |K - K^*| \\
&\quad - \lambda_K |K - K^*| \\
&= -\lambda_s \|\mathbf{s}\|_2 - |K - K^*| \left(-\frac{\|\mathbf{s}\|_2}{m} + \frac{1}{\gamma} \dot{K} - \lambda_K \right) \\
&\quad - \lambda_K |K - K^*| \\
&< -\lambda_s \|\mathbf{s}\|_2 - |K - K^*| \left(-\frac{\|\mathbf{s}\|_2}{m_{min}} + \frac{1}{\gamma} \dot{K} - \lambda_K \right) \\
&\quad - \lambda_K |K - K^*| \\
&= -\lambda_s \|\mathbf{s}\|_2 - \lambda_K |K - K^*| - L
\end{aligned} \tag{54}$$

where $L \triangleq |K - K^*| \left(-\frac{\|\mathbf{s}\|_2}{m_{min}} + \frac{1}{\gamma} \dot{K} - \lambda_K \right)$. We write Eq. (54) as

$$\begin{aligned}
\dot{V} &< -\lambda_s \|\mathbf{s}\|_2 - \lambda_K |K - K^*| - L \\
&= -\lambda_s \sqrt{2} \cdot \frac{\|\mathbf{s}\|_2}{\sqrt{2}} - \lambda_K \sqrt{2\gamma} \cdot \frac{|K - K^*|}{\sqrt{2\gamma}} - L \\
&\leq -\min \left(\lambda_s \sqrt{2}, \lambda_K \sqrt{2\gamma} \right) \cdot \left(\frac{\|\mathbf{s}\|_2}{\sqrt{2}} + \frac{|K - K^*|}{\sqrt{2\gamma}} \right) - L \\
&\leq -\lambda \cdot V^{1/2} - L
\end{aligned} \tag{55}$$

where $\lambda \triangleq \sqrt{2} \min (\lambda_s, \lambda_K \sqrt{\gamma}) > 0$.

The parameter L could be positive by selecting a proper γ . The positive condition $L > 0$ is equivalent to

$$\gamma < \frac{m_{min} \dot{K}}{\lambda_K m_{min} + \|\mathbf{s}\|_2} \tag{56}$$

Using Eqs. (39-40) and the conditions $\|\mathbf{s}\|_2 > \varepsilon$ and $K \geq K_0$, it can be readily shown that

$$\gamma < \frac{\eta m_{min} K_0}{\lambda_K m_{min} + \varepsilon} \tag{57}$$

If the parameter L is always positive, we can conclude that $\dot{V} < -\lambda V^{1/2} - L < -\lambda V^{1/2}$. Hence the sliding surface converges into the region $\|\mathbf{s}\|_2 \leq \varepsilon$ in a finite-time by lemma 2. ■

Lemma 3. When the sliding variable is bounded as $\|\mathbf{s}\|_2 \leq \varepsilon$, the bound on the relative position error is derived from the definition of the sliding variable as $\|\mathbf{r}_e\|_2 \leq \|\mathbf{R}\|_2$ where $\mathbf{R} = [R_1 \ R_2 \ R_3]$. R_i is the unique solution of the equation $f(R_i) = 0$, where $f(x) = \varepsilon_i - \alpha_i \text{sig}^\rho x - \beta_i x$ and $|s_i| \leq \varepsilon_i$ for $i = 1, 2, 3$.

Proof:

Let us define the Lyapunov function $V = \frac{1}{2} \mathbf{r}_{ei}^2$, then the time derivative is derived as

$$\dot{V} = \mathbf{r}_{ei} \dot{\mathbf{r}}_{ei} \tag{58}$$

The bound on the sliding surface $|s_i| \leq \varepsilon_i$ constrains $\dot{\mathbf{r}}_{ei}$ as

$$g(x) \leq \dot{\mathbf{r}}_{ei} \leq f(x) \tag{59}$$

where $f(x) = \varepsilon_i - \alpha_i \text{sig}^\rho x - \beta_i x$ and $g(x) = -\varepsilon_i - \alpha_i \text{sig}^\rho x - \beta_i x$.

$$f(x) = \begin{cases} \varepsilon_i + \alpha_i (-x)^\rho + \beta_i (-x) > 0 & \text{if } x < 0, \\ \varepsilon_i > 0 & \text{if } x = 0, \\ \varepsilon_i - \alpha_i x^\rho - \beta_i x & \text{if } x > 0. \end{cases} \tag{60}$$

$$\frac{df(x)}{dx} = -\rho \alpha_i |x|^{\rho-1} - \beta_i < 0 \quad \text{for } \forall x \in \mathbb{R}. \tag{61}$$

Since $f(0) > 0$, $f(x) > 0$ for $\forall x \in \mathbb{R}^-$ and monotonically decreases for $\forall x \in \mathbb{R}$, it is obvious that there exists a unique positive solution $R_{i,p} \in \mathbb{R}^+$ such that $f(R_{i,p}) = 0$. It derives the sign of $f(x)$ is calculated as

$$\begin{cases} f(x) > 0 & \text{for } x < R_{i,p}, \\ f(x) = 0 & \text{for } x = R_{i,p} > 0, \\ f(x) < 0 & \text{for } x > R_{i,p} > 0. \end{cases} \tag{62}$$

On the other hand, $g(x) = f(x) - 2\varepsilon_i$, which means $g(x)$ translates $f(x)$ parallel to y direction as $-2\varepsilon_i$.

$$g(x) = \begin{cases} -\varepsilon_i + \alpha_i (-x)^\rho + \beta_i (-x) & \text{if } x < 0, \\ -\varepsilon_i < 0 & \text{if } x = 0, \\ -\varepsilon_i - \alpha_i x^\rho - \beta_i x < 0 & \text{if } x > 0. \end{cases} \tag{63}$$

$$\frac{dg(x)}{dx} = \frac{df(x)}{dx} < 0. \tag{64}$$

Likewise, the sign of $g(x)$ is determined according to $R_{i,n} \in \mathbb{R}^-$ which is the unique solution of $g(R_{i,n}) = 0$.

$$\begin{cases} g(x) > 0 & \text{for } x < R_{i,n} < 0, \\ g(x) = 0 & \text{for } x = R_{i,n} < 0, \\ g(x) < 0 & \text{for } x > R_{i,n}. \end{cases} \tag{65}$$

As a result, substitution of Eq. (62,65) to Eq. (59) derives

$$\begin{cases} g(x) \leq \dot{\mathbf{r}}_{ei} \leq f(x) < 0 & \text{if } 0 < R_{i,p} < x \\ 0 < g(x) \leq \dot{\mathbf{r}}_{ei} \leq f(x) & \text{if } x < R_{i,n} < 0 \end{cases} \tag{66}$$

The parallel translation of $f(x)$ and $g(x)$ derives the relationship between $R_{i,p}$ and $R_{i,n}$ as

$$\begin{aligned} g(R_{i,n}) &= -\varepsilon_i - \alpha_i \text{sig}^\rho R_{i,n} - \beta_i R_{i,n} \\ &= -\varepsilon_i + \alpha_i (-R_{i,n})^\rho + \beta_i (-R_{i,n}) \\ &= f(-R_{i,n}) \\ &= 0 \end{aligned} \quad (67)$$

It suggests that $R_{i,p} = -R_{i,n} = R_i$ because the solutions are unique. The time derivative of the Lyapunov function in Eq. (58) become negative when $|r_{ei}| > R_i$ as

$$\dot{V} = r_{ei} \dot{r}_{ei} < 0 \quad (68)$$

which proves that the region $\mathbb{L} = \{r_{ei} \in \mathbb{R} \mid |r_{ei}| \leq R_i\}$ is the domain of attraction.

B. Attitude Control System

Sliding variable design

The sliding variable for the attitude control system is designed based on nonsingular fast terminal sliding mode as follows:

$$s_{att} = \omega_e + \alpha_{att} \text{sig}^{\rho_{att}} q_{ev} + \beta_{att} q_{ev} \quad (69)$$

where the definition of $\text{sig}^\rho \xi$ is the same with the one in Eq. (41).

Proposition 2. *The quaternion and angular velocity error (q_{ev}, ω_e) are asymptotically stable if the sliding variable s in Eq. (69) is zero.*

Proof:

Let us define the Lyapunov candidate as [47]

$$V = q_{ev}^T q_{ev} + (1 - q_{e4})^2 \quad (70)$$

, then the time derivative \dot{V} is derived as

$$\dot{V} = -2\dot{q}_{e4} = q_{ev}^T \omega_e \quad (71)$$

Since the attitude sliding variable is assumed to be zero, then it is derived by substituting Eq. (69)

$$\begin{aligned} \dot{V} &\leq q_{ev}^T (-\alpha \text{sig}^\rho q_{ev} - \beta q_{ev}) \\ &\leq -\alpha_{min} q_{ev}^T \text{sig}^\rho q_{ev} - \beta_{min} q_{ev}^T q_{ev} \\ &\leq -\alpha_{min} \|q_{ev}\|_2^{\rho+1} - \beta_{min} \|q_{ev}\|_2^2 \\ &= -\alpha_{min} V^{\frac{\rho+1}{2}} - \beta_{min} V \end{aligned} \quad (72)$$

where $\alpha_{min} = \min_{i=1,2,3} \alpha_i$ and $\beta_{min} = \min_{i=1,2,3} \beta_i$.

Therefore when the attitude sliding variable is retained at zero, the quaternion error converge to zero. If the sliding variable and the quaternion error are zero, the angular velocity error is also zero according to the definition of the sliding variable in Eq. (69). As a result, lemma 1 proves the finite-time stability of the quaternion and angular velocity errors when the sliding surface is zero. ■

Theorem 2.

Consider the attitude control system that is nonlinear and uncertain Eq. (24) with the adaptive smooth feedback control Eq. (39,40) where p of the adaptive law is 2 and

the sliding manifold is designed as Eq. (69). If $\|s\|_2 > \varepsilon$, then the attitude states converge to the region $\|s\|_2 \leq \varepsilon$ in a finite time.

Proof:

The Lyapunov candidate is defined as

$$V = \frac{1}{2} s^T J_0 s + \frac{1}{2\gamma_{att}} (K - K_{att}^*)^2 \quad (73)$$

where γ_{att} is a positive constant and K_{att}^* is also a positive constant satisfying $K_{att}(t) < K_{att}^*$. By the definition of the sliding variable Eq. (69), its time derivative is described as

$$\dot{s} = \ddot{q}_{ev} + (\rho \alpha \Theta + \beta) \dot{q}_{ev} \quad (74)$$

where $\Theta = \text{diag} \{|q_{e1}|^{\rho-1}, |q_{e2}|^{\rho-1}, |q_{e3}|^{\rho-1}\}$ is positive semi-definite. By substituting Eq. (30) into Eq. (29), the second derivative of quaternion error can be described in the error dynamic equation as

$$\begin{aligned} \ddot{q}_{ev} &= \frac{1}{2} [(\dot{q}_{e4} \mathbf{I}_{3 \times 3} + \dot{q}_{ev}^\times) \omega_e + (q_{e4} \mathbf{I}_{3 \times 3} + q_{ev}^\times) \dot{\omega}_e] \\ &= \frac{1}{2} [(\dot{q}_{e4} \mathbf{I}_{3 \times 3} + \dot{q}_{ev}^\times) \omega_e + (q_{e4} \mathbf{I}_{3 \times 3} + q_{ev}^\times) \mathbf{J}^{-1} \\ &\quad \left[-(\omega_e + \mathbf{C}_r^b \omega_r) \times (\mathbf{J}(\omega_e + \mathbf{C}_r^b \omega_r) + \mathbf{J}_w \omega_w) \right. \\ &\quad \left. + \mathbf{u} + \mathbf{d} + \mathbf{J}(\omega_e^\times \mathbf{C}_r^b \omega_r - \mathbf{C}_r^b \dot{\omega}_r) \right]] \end{aligned} \quad (75)$$

The momentum of inertia is decomposed as Eq. (36), and the inverse matrix is derived as

$$\mathbf{J}^{-1} = (\mathbf{J}_0 + \delta \mathbf{J})^{-1} = \mathbf{J}_0^{-1} + \delta \hat{\mathbf{J}} \quad (76)$$

where $\delta \hat{\mathbf{J}} = -\mathbf{J}_0^{-1} \delta \mathbf{J} (\mathbf{I}_{3 \times 3} + \mathbf{J}_0^{-1} \delta \mathbf{J})^{-1} \mathbf{J}_0^{-1}$ [36], [48].

Hence the part of the second term of Eq. (75) can be decomposed into

$$\begin{aligned} &\mathbf{J}^{-1} \left[-(\omega_e + \mathbf{C}_r^b \omega_r) \times (\mathbf{J}(\omega_e + \mathbf{C}_r^b \omega_r) + \mathbf{J}_w \omega_w) \right. \\ &\quad \left. + \mathbf{u} + \mathbf{d} + \mathbf{J}(\omega_e^\times \mathbf{C}_r^b \omega_r - \mathbf{C}_r^b \dot{\omega}_r) \right] \\ &= (\mathbf{J}_0^{-1} + \delta \hat{\mathbf{J}}) \left[-(\omega_e + \mathbf{C}_r^b \omega_r) \times (\mathbf{J}_0 + \delta \mathbf{J})(\omega_e + \mathbf{C}_r^b \omega_r) \right. \\ &\quad \left. + \mathbf{J}_w \omega_w + \mathbf{u} + \mathbf{d} + (\mathbf{J}_0 + \delta \mathbf{J})(\omega_e^\times \mathbf{C}_r^b \omega_r - \mathbf{C}_r^b \dot{\omega}_r) \right] \\ &= \mathbf{J}_0^{-1} \left[-(\omega_e + \mathbf{C}_r^b \omega_r) \times \mathbf{J}_0(\omega_e + \mathbf{C}_r^b \omega_r) \right. \\ &\quad \left. - (\omega_e + \mathbf{C}_r^b \omega_r) \times \mathbf{J}_w \omega_w + \mathbf{u} + \mathbf{J}_0(\omega_e^\times \mathbf{C}_r^b \omega_r - \mathbf{C}_r^b \dot{\omega}_r) \right] \\ &\quad + \mathbf{J}_0^{-1} \left[-(\omega_e + \mathbf{C}_r^b \omega_r) \times \delta \mathbf{J}(\omega_e + \mathbf{C}_r^b \omega_r) \right. \\ &\quad \left. + \delta \mathbf{J}(\omega_e^\times \mathbf{C}_r^b \omega_r - \mathbf{C}_r^b \dot{\omega}_r) \right] \\ &\quad + \delta \hat{\mathbf{J}} \left[-(\omega_e + \mathbf{C}_r^b \omega_r) \times \mathbf{J}_0(\omega_e + \mathbf{C}_r^b \omega_r) \right. \\ &\quad \left. - (\omega_e + \mathbf{C}_r^b \omega_r) \times \delta \mathbf{J}(\omega_e + \mathbf{C}_r^b \omega_r) \right. \\ &\quad \left. - (\omega_e + \mathbf{C}_r^b \omega_r) \times \mathbf{J}_w \omega_w + \mathbf{u} + \mathbf{d} \right. \\ &\quad \left. + \mathbf{J}_0(\omega_e^\times \mathbf{C}_r^b \omega_r - \mathbf{C}_r^b \dot{\omega}_r) \right. \\ &\quad \left. + \delta \mathbf{J}(\omega_e^\times \mathbf{C}_r^b \omega_r - \mathbf{C}_r^b \dot{\omega}_r) \right] \end{aligned} \quad (77)$$

$$\begin{aligned}
&= \mathbf{J}_0^{-1} \mathbf{u} + \mathbf{J}_0^{-1} \left[- \left(\omega_e + \mathbf{C}_r^b \omega_r \right) \times \mathbf{J}_0 \left(\omega_e + \mathbf{C}_r^b \omega_r \right) \right. \\
&\quad \left. - \left(\omega_e + \mathbf{C}_r^b \omega_r \right) \times \mathbf{J}_w \omega_w + \mathbf{J}_0 \left(\omega_e^\times \mathbf{C}_r^b \omega_r - \mathbf{C}_r^b \omega_r \right) \right] \\
&\quad + \mathbf{J}_0^{-1} \left[- \left(\omega_e + \mathbf{C}_r^b \omega_r \right) \times \delta \mathbf{J} \left(\omega_e + \mathbf{C}_r^b \omega_r \right) \right. \\
&\quad \left. + \mathbf{d} + \delta \mathbf{J} \left(\omega_e^\times \mathbf{C}_r^b \omega_r - \mathbf{C}_r^b \omega_r \right) \right] \\
&\quad + \delta \hat{\mathbf{J}} \left[- \left(\omega_e + \mathbf{C}_r^b \omega_r \right) \times \mathbf{J}_0 \left(\omega_e + \mathbf{C}_r^b \omega_r \right) \right. \\
&\quad \left. - \left(\omega_e + \mathbf{C}_r^b \omega_r \right) \times \delta \mathbf{J} \left(\omega_e + \mathbf{C}_r^b \omega_r \right) \right. \\
&\quad \left. - \left(\omega_e + \mathbf{C}_r^b \omega_r \right) \times \mathbf{J}_w \omega_w \right. \\
&\quad \left. + \mathbf{u} + \mathbf{d} + \mathbf{J}_0 \left(\omega_e^\times \mathbf{C}_r^b \omega_r - \mathbf{C}_r^b \omega_r \right) \right] \\
&= \mathbf{J}_0^{-1} \mathbf{u} + \bar{\mathbf{d}}_1 + \bar{\mathbf{d}}_2 + \bar{\mathbf{d}}_3
\end{aligned} \tag{78}$$

where $\bar{\mathbf{d}}_1$, $\bar{\mathbf{d}}_2$, and $\bar{\mathbf{d}}_3$ are the first, second, and third terms of Eq. (78).

Therefore, Eq. (74) substituted by Eq. (75, 77) is derived as

$$\begin{aligned}
\dot{\mathbf{s}} &= \mathbf{J}_0^{-1} \mathbf{u} + \bar{\mathbf{d}}_1 + \bar{\mathbf{d}}_2 + \bar{\mathbf{d}}_3 \\
&\quad + \frac{1}{2} (\rho \boldsymbol{\alpha} \boldsymbol{\Theta} + \boldsymbol{\beta} \mathbf{I}_{3 \times 3}) (q_{e4} \mathbf{I}_{3 \times 3} + \mathbf{q}_{ev}^\times) \omega_e \\
&= \mathbf{J}_0^{-1} \mathbf{u} + \bar{\mathbf{d}}_1 + \bar{\mathbf{d}}_2 + \bar{\mathbf{d}}_3 + \bar{\mathbf{d}}_4 \\
&= \mathbf{J}_0^{-1} \mathbf{u} + \lambda_{max}^{-1} \bar{\mathbf{d}}
\end{aligned} \tag{79}$$

where $\lambda_{min}^{-1} \bar{\mathbf{d}} = \bar{\mathbf{d}}_1 + \bar{\mathbf{d}}_2 + \bar{\mathbf{d}}_3 + \bar{\mathbf{d}}_4$.

As a result, the time derivative of the Lyapunov function in Eq. (73) leads to

$$\begin{aligned}
\dot{V} &= \mathbf{s}^T \mathbf{J}_0 \dot{\mathbf{s}} + \frac{1}{\gamma} (K - K^*) \dot{K} \\
&= \mathbf{s}^T \left(\mathbf{u} + \lambda_{max}^{-1} \mathbf{J}_0 \bar{\mathbf{d}} \right) + \frac{1}{\gamma} (K - K^*) \dot{K} \\
&= \mathbf{s}^T \left(-\frac{K}{\varepsilon} \mathbf{s} + \lambda_{max}^{-1} \mathbf{J}_0 \bar{\mathbf{d}} \right) + \frac{1}{\gamma} (K - K^*) \dot{K} \\
&\leq \lambda_{max}^{-1} \mathbf{s}^T \mathbf{J}_0 \bar{\mathbf{d}} - \frac{K}{\varepsilon} \mathbf{s}^T \mathbf{s} + \frac{1}{\gamma} (K - K^*) \dot{K}
\end{aligned} \tag{80}$$

Since \mathbf{J}_0 is a symmetric matrix, the inequality equation is derived by spectral theorem

$$\mathbf{s}^T \mathbf{J}_0 \bar{\mathbf{d}} \leq \lambda_{max} \|\mathbf{s}\|_2 \|\bar{\mathbf{d}}\|_2 \tag{81}$$

where λ_{max} is the maximum eigenvalue of \mathbf{J}_0 . It follows that

$$\begin{aligned}
\dot{V} &\leq \|\mathbf{s}\|_2 \|\bar{\mathbf{d}}\|_2 - \frac{K}{\varepsilon} \|\mathbf{s}\|_2^2 + \frac{1}{\gamma} (K - K^*) \dot{K} \\
&< \|\mathbf{s}\|_2 \left(D - \frac{K}{\varepsilon} \|\mathbf{s}\|_2 \right) + \frac{1}{\gamma} (K - K^*) \dot{K}
\end{aligned} \tag{82}$$

where $\|\bar{\mathbf{d}}\|_2 < D$. In the region $\|\mathbf{s}\|_2 > \varepsilon$, then

$$\begin{aligned}
\dot{V} &< \|\mathbf{s}\|_2 (D - K) + \frac{1}{\gamma} (K - K^*) \dot{K} \\
&= -\beta_s \|\mathbf{s}\|_2 + \frac{1}{\gamma} (K - K^*) \dot{K}
\end{aligned} \tag{83}$$

where $\beta_s = K - D$ should be positive and it constrains the control gain as $K(t) \geq K_0 > D$.

$$\begin{aligned}
\dot{V} &< -\beta_s \|\mathbf{s}\|_2 - \frac{1}{\gamma} |K - K^*| + \beta_K |K - K^*| - \beta_K |K - K^*| \\
&= -\beta_s \|\mathbf{s}\|_2 - |K - K^*| \left(\frac{1}{\gamma} \dot{K} - \beta_K \right) - \beta_K |K - K^*| \\
&= -\beta_s \|\mathbf{s}\|_2 - \beta_K |K - K^*| - \kappa
\end{aligned} \tag{84}$$

where $K - K^* = -|K - K^*|$ because $K \leq K^*$ and $\kappa \triangleq |K - K^*| \left(\frac{1}{\gamma} \dot{K} - \beta_K \right)$.

As a consequence, it is derived as

$$\begin{aligned}
\dot{V} &< -\beta_s \|\mathbf{s}\|_2 - \beta_K |K - K^*| - \kappa \\
&= -\beta_s \cdot \frac{\sqrt{2}}{\lambda_{max}^{1/2}} \cdot \frac{\lambda_{max}^{1/2}}{\sqrt{2}} \\
&\quad - \beta_K \cdot \sqrt{2\gamma} \cdot \frac{1}{\sqrt{2\gamma}} |K - K^*| - \kappa \\
&\leq -\sqrt{2} \min \left(\frac{\beta_s}{\lambda_{max}^{1/2}}, \beta_K \sqrt{\gamma} \right) \\
&\quad \cdot \left(\frac{1}{\sqrt{2}} \lambda_{max}^{1/2} \|\mathbf{s}\|_2 + \frac{1}{\sqrt{2\gamma}} |K - K^*| \right) - \kappa \\
&\leq -\beta \cdot V^{1/2} - \kappa
\end{aligned} \tag{85}$$

where $\beta \triangleq \sqrt{2} \min \left(\frac{\beta_s}{\lambda_{max}^{1/2}}, \beta_K \sqrt{\gamma} \right) > 0$.

The positiveness of parameter κ suggests that the γ must be selected properly. If $\kappa > 0$, it yields

$$\frac{1}{\gamma} \dot{K} - \beta_K > 0 \Rightarrow \gamma < \frac{\dot{K}}{\beta_K} \tag{86}$$

The adaptive law Eq. (40) is substituted and it derives as

$$\gamma < \eta \frac{K \left(\frac{\|\mathbf{s}\|_2}{\varepsilon} - 1 \right) + K_0}{\beta_K} = \Gamma(t) \tag{87}$$

The adaptive gain has a lower bound as $K(t) \geq K_0$ and if the region $\|\mathbf{s}\|_2 > \varepsilon$ is assumed, then

$$\eta \frac{K_0}{\beta_K} < \eta \frac{K \left(\frac{\|\mathbf{s}\|_2}{\varepsilon} - 1 \right) + K_0}{\beta_K} < \Gamma \tag{88}$$

Therefore, parameter γ must be chosen as

$$\gamma < \eta \frac{K_0}{\beta_K}. \tag{89}$$

Eq. (85) shows that the Lyapunov function satisfies $\dot{V} \leq -\beta \cdot V^{1/2} - \kappa < -\beta \cdot V^{1/2}$. The finite time convergence of the sliding surface in the region $\|\mathbf{s}\|_2 \leq \varepsilon$ is guaranteed by lemma 2. ■

V. Simulation Results

The α and β are sliding surface parameters and adjust the weights between the error and its time derivative. If $\alpha_{att,i}$, $\beta_{att,i}$, ρ_{att} , $\alpha_{orb,i}$, $\beta_{orb,i}$ and ρ_{orb} are set as 1.44, 1.44, 1.10, $7.00e-03$, $7.00e-03$ and 1.90 for $i = 1, 2, 3$, then the error and its time derivative have the same order.

TABLE I

Simulation parameters for attitude and orbit control systems

ρ_{att}	α_{att}	β_{att}	ε_{att}
1.10	1.44	1.44	$6.00e-02$
$K_{att}(0)$	$K_{att,0}$	η_{att}	
$2.00e-04$	$2.00e-07$	$5.00e-02$	
ρ_{orb}	α_{orb}	β_{orb}	ε_{orb}
1.90	$7.00e-03$	$7.00e-03$	$1.20e-02$
$K_{orb}(0)$	$K_{orb,0}$	η_{orb}	
$3.00e-05$	$1.00e-08$	$3.00e-04$	

The smaller ε induces the sliding surface to converge into the smaller region, which suggests the smaller error. However, the proper epsilon must be chosen considering the requirements in error and the control input saturation. ε_{att} and ε_{orb} are set as $6.00e-02$ and $1.20e-02$, respectively. The control parameters η_{att} , $K_{att}(0)$, $K_{att,0}$, η_{orb} , $K_{orb}(0)$ and $K_{orb,0}$ are $5.00e-02$, $2.00e-04$, $2.00e-07$, $3.00e-04$, $3.00e-05$ and $1.00e-08$. These parameters are summarized in table I.

According to the top panel of Fig.5, the two-norm of the orbital sliding surface rapidly decreases within 50 seconds, and initially converges below ε_{orb} at 330-365 seconds. It stays in the region ε_{orb} after 430 seconds. Even though the sliding surface temporarily overshoots ε_{orb} during 415-430 seconds, the appropriate choice of α_{orb} and β_{orb} holds the two norm of the position errors below 3 meters. The two-norm of the position error suggested in the middle panel of Fig.5 initially reduces below the requirement at 41.36 sec, and then remains in the region thereafter.

The position errors in each direction of the LVLH frame are described at the bottom panel. The radial position error stays at $-\sqrt{3}$ meters once it is stabilized. The along-track and cross-track position errors reach zero at about 400 seconds when the sliding surface converges. The along-track position error slowly increases to $\sqrt{3}$ at the end of the simulation. On the other hand, the cross-track position error remains near zero thereafter.

The onboard algorithm generates the reference thrust ($\mathbf{u}_{orb,r}$) in the LVLH frame. The reference thrust is converted to the reference body frame and allocated to the four nozzles of the propulsion system. The attitude control error between the reference and current body frames contributes to the error in thrust firing. The fired thrust (\mathbf{u}_{orb}) and the thrust error ($\mathbf{u}_{orb,e} = \mathbf{u}_{orb} - \mathbf{u}_{orb,r}$) that are converted to the LVLH frame are depicted in top three panels of Fig.6. The radial thrust error in the first panel has a positive value and rapidly decreases during the first 50 seconds. The positive thrust error suggests that the reference thrust is negative and controls the positive orbital error. It also explains the positive along-track and cross-track thrust errors in the second and third panels. After 50 seconds, the magnitude of thrust is almost zero and induces the offset of the radial position error. After the convergence of the sliding variable, only a small

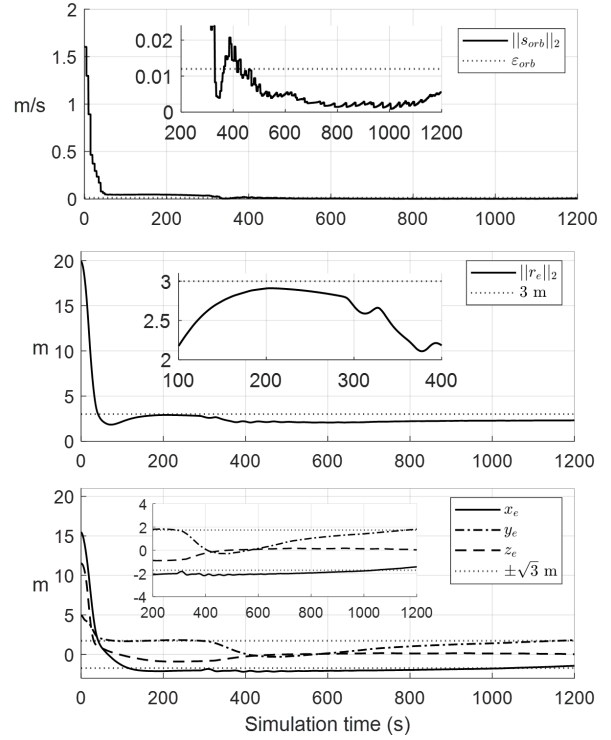


Fig. 5. Two-norm of the orbital sliding surface and position error

magnitude of thrust is fired discontinuously. Because the propulsion system has a thrust resolution of 0.01 mN, the thrust could be fired once the reference thrust is large enough. Compared to the radial and along-track thrusts, the cross-track thrust easily controls the position error and consumes less fuel after the convergence.

The adaptive rule could be reorganized as Eq.(90).

$$\dot{K}(t) = \eta K \left(\left\| -\frac{s}{\varepsilon} \right\|_2 - \left(1 - \frac{K_0}{K} \right) \right) \quad (90)$$

If the sliding surface is bounded as $\|s\|_2 \leq (1 - \frac{K_0}{K})\varepsilon$, then $\dot{K} < 0$ and the K decreases. Since $\|s\|_2 \leq (1 - \frac{K_0}{K})\varepsilon < \varepsilon$, the sign of \dot{K} and the fluctuation of K indicate the boundedness of the sliding surface. The fourth and fifth panels in Fig.6 depict \dot{K} and K . These simulation results confirm that the sliding variable is bounded after 430 seconds.

The abrupt rises in the sliding surface and quaternion errors occur when the reference quaternion changes. According to the simulation result shown in Fig.7, the two reference quaternions switch 32 times for 1200 seconds. The expectable reference quaternions make it possible to predict the convergence speed of the attitude sliding surface. The initial attitude is usually oriented far from the reference attitude in the beginning. The top two panels in Fig.7 show that the change in the reference attitude could instantly reduce the control error during the first 50 seconds. The ROCS generates the reference thrusts more frequently before the orbital sliding mode converges at 430 seconds. The attitude maneuver is very regular and the convergence speed of the attitude sliding surface

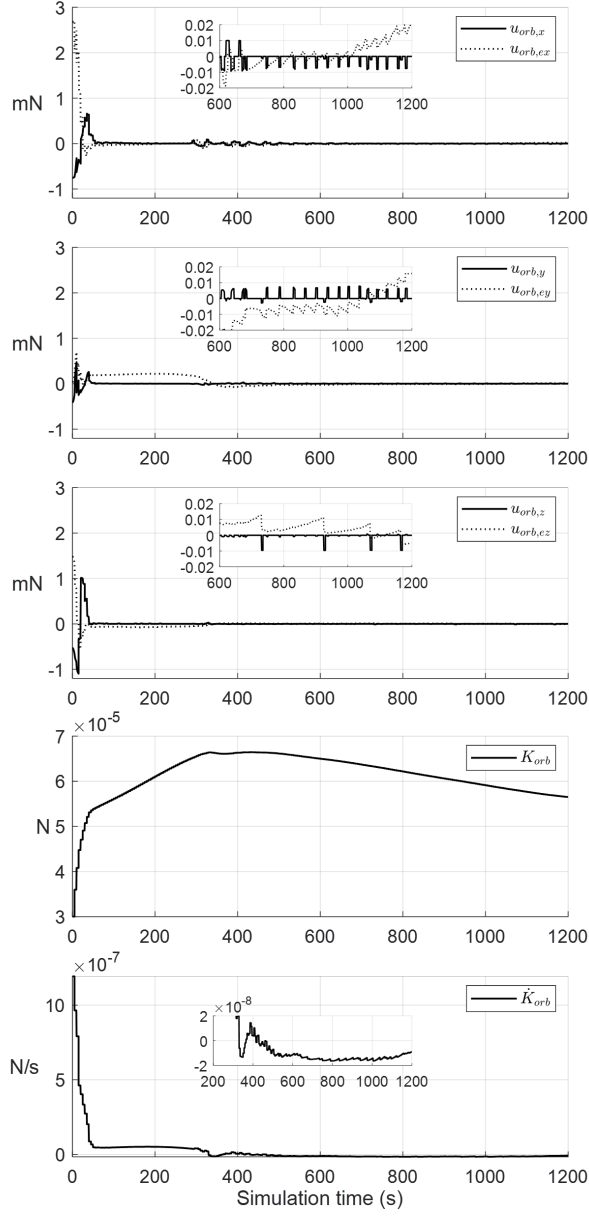


Fig. 6. Fired thrust, thrust error, orbital control gain and its time derivative

should be analyzed after 430 seconds. The attitude sliding surface is bounded by $\|s\|_2 \leq \varepsilon_{att}$ within 7.98 s on average after 430 seconds including 38.20 s at the last control.

As it is described in section II, the reference attitude rotates ± 10 deg along the $+\hat{b}_x$ axis to achieve the controllability in $+\hat{b}_z$ axis. Therefore, only the q_{e1} in the second panel momentarily increases except for the initial 50 seconds. Since the three components of the quaternion vector are coupled by the cross term in Eq. (25), the increase in q_{e1} causes q_{e2} and q_{e3} to fluctuate (the third and fourth panels).

The control torque profile in the top three panels in Fig.8 corresponds to the trends of the quaternion errors. $u_{att,1}$ is temporarily saturated for about 10 seconds when

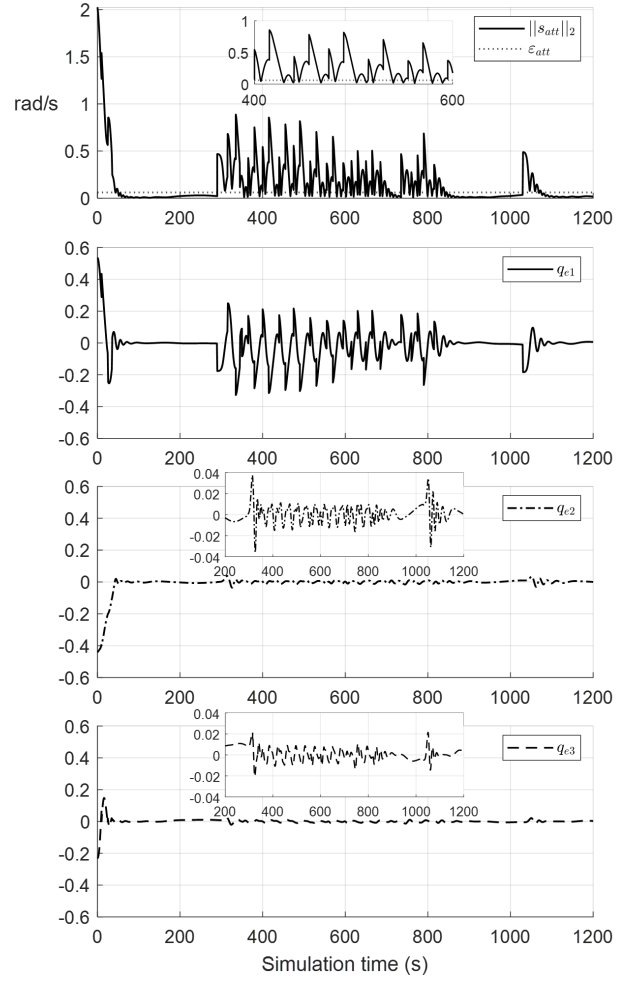


Fig. 7. Two-norm of the attitude sliding surface and quaternion error

the q_{e1} is at the peak. $u_{att,2}$ and $u_{att,3}$ are relatively small but never zero unless the three components in quaternion error vectors become zero simultaneously. The fourth and fifth panels explain the rationale that the last convergence speed of the attitude sliding variable is latent. The attitude sliding variable stays in the region below ε_{att} for about 200 seconds before the last control (top panel of Fig.7). Theoretically, \dot{K} is negative when $\|s\|_2 \leq \left(1 - \frac{K_0}{K}\right) \cdot \varepsilon_{att}$ and the simulation verifies that they are only 0.12 s different. Hence, \dot{K} is negative for considerable time and it provokes the significant reduction of K in the fourth panel.

VI. Conclusion

The virtual telescope demonstration mission requires precise control performance in both attitude and relative orbit control systems. Since the propulsion system has only two degrees of freedom, the attitude control performance could degrade the mission success possibility. In this paper, the nonsingular fast terminal sliding surface and the adaptive smooth controller are introduced to the attitude and relative orbit control system. The

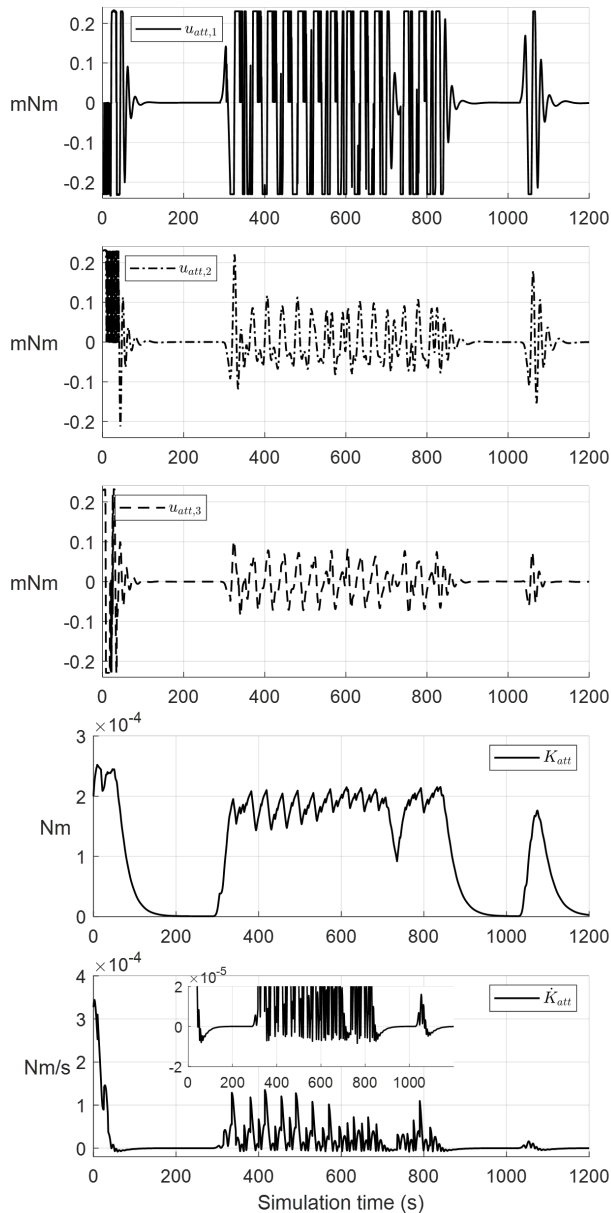


Fig. 8. Control torque, attitude control gain and its time derivative

nonsingular fast terminal sliding mode naturally has a fast convergence rate and improves the aligned time. The control law is designed to have continuous signals and prevents the system from chattering—the radical problem of the classical sliding mode. The adaptive rule designed based on the vector norm of the sliding surface is able to consider the changes in the sliding surface. The simulation results show that the adaptive smooth controller based on the nonsingular fast terminal sliding mode dramatically improves the control performance with reasonable thrust consumption.

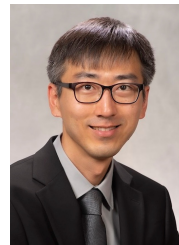
REFERENCES

- [1] M. D'Errico Distributed Space Missions for Earth System Monitoring *Springer Science+Business Media New York*, 2013
- [2] F. Kamalabadi, E. Lightsey, D. Rabin, A. Daw, S. D'Amico, A. Koenig, P. Chamberlin, T. Woods, S. Gupta, E. Ekici, J. Sample, H. Park, A. Alexeenko, J. Hwang, K. Denis, J. Klimchuk Distributed Space Telescopes Enabled by Constellation of Small Satellites *AGU Fall Meeting 2021, held in New Orleans, LA*, 13-17 December 2021
- [3] B. A. Corbin The Values Proposition of Distributed Satellite Systems for Space Science Missions *Ph.D Thesis*, Department of Aeronautics and Astronautics, Massachusetts Institute of Technology, 2015
- [4] B. D. Tapley, S. Bettadpur, M. M. Watkins, and C. Reigber The gravity recovery and climate experiment: Mission overview and early results *Geophysical Research Letters*, vol.31, no.9, May 2004, doi: [10.1029/2004GL019920](https://doi.org/10.1029/2004GL019920)
- [5] R. P. Kornfeld, B. W. Arnold, M. A. Gross, N. T. Dahya, W. M. Klipstein, P. F. Gath, and S. Bettadpur GRACE-FO: The Gravity Recovery and Climate Experiment Follow-On Mission *Journal of Spacecraft and Rockets*, vol.56, no.3, May 2019, doi: [10.2514/1.A34326](https://doi.org/10.2514/1.A34326)
- [6] A. Moreira, G. Kireger, I. Hajnsek, D. Hounam, M. Werner, S. Riegger, and E. Settlemyer TanDEM-X: A TerraSAR-X Add-On Satellite for Single-Pass SAR interferometry *Geosci. and remote Sens. Symp.* 2, 2004, doi: [10.1109/IGARSS.2004.1368578](https://doi.org/10.1109/IGARSS.2004.1368578)
- [7] N. H. Roth Navigation and Control Design for the CanX-4/-5 Satellite Formation Flying Mission *M.S. Thesis*, University of Toronto, Toronto, Canada, 2011
- [8] G. Bonin, N. Roth, S. Armitage, J. Newman, B. Risi, and R. E. Zee CanX-4 and CanX-5 Precision Formation Flight: Mission Accomplished! *29th Annual AIAA/USU Conference on Small Satellites*, pp.1–15, 2015
- [9] C.W.T. Roscoe, J.J. Westphal, and E. Mosleh Overview and GNC design of the CubeSat Proximity Operations Demonstration (CPOD) mission *Acta Astronaut.*, vol.153, pp.410–421, 2018 doi: [10.1016/j.actaastro.2018.03.033](https://doi.org/10.1016/j.actaastro.2018.03.033)
- [10] A. W. Koenig, B. Macintosh and S. D'Amico Formation Design of Distributed Telescopes in Earth Orbit for Astrophysics Applications *Journal of Spacecraft and Rockets*, vol.56, no.5, Sep-Oct. 2019, doi: [10.2514/1.A34420](https://doi.org/10.2514/1.A34420)
- [11] P. C. Calhoun, A.-M. Novo-Gradac, and N. Shah Spacecraft alignment determination and control for dual spacecraft precision formation flying *Acta Astronaut.*, vol.153, pp.349–356, 2018 doi: [10.1016/j.actaastro.2018.02.021](https://doi.org/10.1016/j.actaastro.2018.02.021)
- [12] Air Force Research Inst. Technology Horizons: A Vision for Air Force Science and Technology 2010-30 AF/ST-TR-10-01-PR, Maxwell AFB, AL, Air Univ. Press, 2010.
- [13] G.K. Skinner, Z. Arzoumanian, W.C. Cash, N. Gehrels, K.C. Gendreau, P. Gorenstein, J.F. Krizmanic, M.C. Miller, J.D. Phillips, R.D. Reasenberg, C.S. Reynolds, R.M. Sambruna, R.E. Streitmatter and D.L. Windt The Milli-Arc-Second Structure Imager, MASSIM: A new concept for a high angular resolution x-ray telescope *Proc. SPIE 7011*, 70110T-1-11, 2008, doi: [10.1117/12.789568](https://doi.org/10.1117/12.789568)
- [14] W. Cash, P. Oakley, M. Turnbull, T. Glassman, A. Lo, R. Polidan, S. Kilston and C. Noecker The New Worlds Observer: scientific and technical advantages of external occulter *Proc. of SPIE 7010*, 70101Q-1-9, 2008 doi: [10.1117/12.789717](https://doi.org/10.1117/12.789717)
- [15] L. Philippe, D. Luc, V. Sebastien and Z. Andrei ASPIICS: a giant coronagraph for the ESA/ PROBA-3 formation flying mission *Proc. of SPIE 7731*, 773118-1-12, 2010, doi: [10.1117/12.858247](https://doi.org/10.1117/12.858247)
- [16] B. R. Dennis, G. K. Skinner, M. J. Li, A. Y. Shih Very High-Resolution Solar X-Ray Imaging Using Diffractive Optics *Sol. Phys.*, vol. 279, pp.573–588, 2012, doi: [10.1007/s11207-012-0016-7](https://doi.org/10.1007/s11207-012-0016-7)
- [17] J.-J. E. Slotine, and W. Li Applied Nonlinear Control *Pearson*, 1991
- [18] V.I. Utkin Sliding Modes in Control and Optimization *Springer-Verlag Berlin, Heidelberg*, 1992
- [19] Y. Shtessel, C. Edwards, L. Fridman, and A. Levant Sliding Mode Control and Observation *Springer New York Heidelberg Dordrecht London*, 2010
- [20] C. Edwards and S. Spurgeon Sliding Mode Control: Theory and Applications *CRC Press*, 1998

- [21] Godard and K. D. Kumar Fault Tolerant Reconfigurable Satellite Formations Using Adaptive Variable Structure Techniques *Journal of Guidance, Control, and Dynamics*, vol. 33, no. 3, pp. 969–984, May–June 2010
- [22] T. Massey and Y. Shtessel Continuous Traditional and High-Order Sliding Modes for Satellite Formation Control *Journal of Guidance, Control, and Dynamics*, vol.28, no.4, pp.826–831, 2005
- [23] R. R. Nair, L. Behera, V. Kumar and M. Jamshidi Multisatellite Formation Control for Remote Sensing Applications Using Artificial Potential Field and Adaptive Fuzzy Sliding Mode Control *IEEE Systems Journal*, vol. 9, no. 2, pp. 508–518, June 2015
- [24] J. Zhou, Q. Hu and M. I. Friswell Decentralized Finite Time Attitude Synchronization Control of Satellite Formation Flying *Journal of Guidance, Control, and Dynamics*, vol.36, no.1 pp.185–195, 2013.
- [25] G. Zeng and M. Hu Finite-time control for electromagnetic satellite formations *Acta Astronautica*, vol.74, pp.120–130, 2012.
- [26] M. AlandiHallaj and N. Assadian Sliding mode control of electromagnetic tethered satellite formation *Advances in Space Research*, vol. 58, pp. 619–634, 2016
- [27] J.-P. Park, S.-Y. Park, Y. Song, G.N. Kim, K. Lee, H.J. Oh, J.-C. Yim, E.J. Lee, S.-H. Hwang, S.W. Kim, K.Y. Choi, D.S. Lee, S.H. Kwon, M.-S. Kim, S.-W. Yeo, T.-H. Kim, S.-H. Lee, K.B. Lee, J.-W. Seo, W.-H. Cho, J. Lee, J.-H. Park, Y.W. Kim, S.J. Kang, J. Hwang, S.H. Lee, J.-H. Yang, S. Jin CubeSat Development for CANYVAL-X Mission *14th International Conferences on Space Operations*, 2016, pp.681–691. doi: 10.5140/JASS.2019.36.4.235.
- [28] G.-N. Kim, S.-Y. Park, T. Lee, D.-E. Kang, S. Jeon, J. Son, N. Kim, Y.-K. Park, Y. Song, Development of CubeSat systems in formation flying for the solar science demonstration: The CANYVAL-C mission *Advances in Space Research*, vol.68, no.11, pp. 4434–4455, 2021 doi: 10.1016/j.asr.2021.09.021.
- [29] H. D. Black A passive system for determining the attitude of a satellite *AIAA Journal*, vol.2, no.7, pp.1350–1351, 1964
- [30] J. R. Wertz *Spacecraft Attitude Determination and Control*
- [31] B. Wie *Space Vehicle Dynamics and Control, 2nd Ed.* Reston, VA, USA: American Institute of Aeronautics and Astronautics, Inc., 2008.
- [32] P. C. Hughes *Space Attitude Dynamics* John Wiley & Sons, 1986
- [33] W. E. Wiesel *Spacecraft Dynamics, 2nd Ed.* McGraw-Hill, 1997
- [34] K. T. Alfriend, S. R. Vadali, P. Gurfill, J. P. How and L. S. Breger *Spacecraft Formation Flying: Dynamics, control and navigation.* Burlington, MA, USA: Elsevier, 2010.
- [35] J. D. Boskovic, S. -M. Li and R. K. Mehra Robust Tracking Control Design for Spacecraft Under Control Input Saturation *Journal of Guidance, Control, and Dynamics*, vol.27, no.4, Aug. 2004, doi: 10.2514/1.1059.
- [36] P. M. Tiwari, S. Janardhanan and M. Nabi Rigid spacecraft attitude control using adaptive integral second order sliding mode *Aerospace Science and Technology*, vol. 42, pp. 50–57, Jan. 2015, doi: 10.1016/j.ast.2014.11.017.
- [37] A. B. Younes, J. D. Turner, D. Mortari and J. L. Junkins A Survey Of Attitude Error Representations *AIAA/AAS Astrodynamics Specialist Conference*, Aug. 2012, doi: 10.2514/6.2012-4422.
- [38] Y. Shi, Q. Hu and L. Guo Attitude Maneuver of Spacecraft With Angular Velocity Constraint *2018 IEEE CSAA Guidance, Navigation and Control Conference (CGNCC)*, pp. 1–5, 2018, doi: 10.1109/GNCC42960.2018.9018957.
- [39] J. Ahmed, V. T. Coppola and D. S. Bernstein Adaptive Asymptotic Tracking of Spacecraft Attitude Motion with Inertia Matrix Identification *Journal of Guidance, Control, and Dynamics*, vol.21, no.5, pp. 684–691, 1998, doi: 10.1109/CDC.1997.657527
- [40] H. Cho, G. Kerschen and T. R. Oliveira Adaptive smooth control for nonlinear uncertain systems *Nonlinear Dyn.*, vol. 99, pp. 2819–2833, Jan. 2020, doi: 10.1007/s11071-019-05446-z.
- [41] S. Yu, X. Yu, B. Shirinzadeh and Z. Man Continuous finite-time control for robotic manipulators with terminal sliding mode *Automatica*, vol. 41, no. 11, pp. 1957–1964, 2005, doi: 10.1016/j.automatica.2005.07.001.
- [42] J. Wang and Z. Sun 6-DOF robust adaptive terminal sliding mode control for spacecraft formation flying *Acta Astronautica*, vol. 74, pp. 76–87, Dec. 2011, doi: 10.1016/j.actaastro.2011.12.005.
- [43] Z. Meng, W. Ren and Z. You Distributed finite-time attitude containment control for multiple rigid bodies *Automatica*, vol. 46, no. 12, pp. 2092–2099, Dec. 2010, doi: 10.1016/j.automatica.2010.09.005.
- [44] S. P. Bhat and D. S. Bernstein Continuous Finite-Time Stabilization of the Translational and Rotational Double Integrators *IEEE Transactions on Automatic Control*, vol. 43 no. 5, pp. 678–682, May 1998, doi: 10.1109/9.668834.
- [45] Y. Hong, J. Wang and D. Cheng Adaptive Finite-Time Control of Nonlinear Systems With Parametric Uncertainty *IEEE Transactions on Automatic Control*, vol. 51, no. 5, pp. 858–862, May 2006, doi: 10.1109/TAC.2006.875006.
- [46] Y. Tang Terminal sliding mode control for rigid robots *Automatica*, vol. 34, no. 1, pp. 51–56, Jan. 1998, doi: 10.1016/S0005-1098(97)00174-X.
- [47] Y.-J. Cheon Sliding Mode Control of Spacecraft with Actuator Dynamics *Transactions on Control, Automation, and Systems Engineering*, vol. 4, no. 2, Jun. 2022
- [48] K. Ma Comments on: Quasi-continuous higher order sliding-mode controllers for spacecraft-attitude-tracking maneuvers *IEEE Trans. Ind. Electron.*, vol. 60, no. 7, pp. 2771–2773, 2013
- [49] S. Jeon, S.-Y. Park and G.-N. Kim Relative Orbit Control Algorithms and Scenarios for the Inertial Alignment Hold Demonstration Mission by CubeSat Formation Flying *Aerospace*, vol. 11, no.2, Feb. 2024, doi: 10.3390/aerospace11020135



Soobin Jeon photograph and biography



Hancheol Cho photograph and biography



Sang-Young Park photograph and biography